Chapter 4
Transonic Wing Design Optimization Based on Evolutionary Algorithm

4.1 Introduction

The objective of this chapter is to ensure the feasibility of the present EA in aerodynamic design optimizations. A transonic wing shape design optimization will be demonstrated. Section 4.2 gives an overview of aerodynamic wing design goals. Formulation of the present design problem is presented in Section 4.3. Sections 4.4 and 4.5 describe the details of the present CFD code and structural model, respectively. Section 4.6 presents the present EA. The design results are shown in Section 4.7.

4.2 Aerodynamic Wing Design Goals

A large part of the maximum takeoff weight of a typical transonic commercial aircraft is occupied by drag-related weights (i.e. fuel and engine size). Therefore, the objective of an aerodynamic optimization of a transonic wing is, in principle, minimization of its drag. Total drag of a transonic wing is composed of pressure drag, skin friction drag, induced drag, and wave drag. Because skin friction drag is mainly determined by the aircraft's total surface area and the friction coefficient, if a planform shape and the flow conditions are given, the design goals of a transonic wing shape optimization are usually minimizations of the other drag components, i.e., pressure drag, induced drag, and wave drag.

Pressure drag is derived from the net component of a surface pressure distribution in the horizontal direction. Although this drag component is usually smaller than the other, flow separation on the upper surface of a wing can drastically increase the pressure drag. Hence, one important design goal is to reduce pressure drag by realizing fully attached flow.

Reduction of the induced drag associating with the wing-tip vortices is another significant factor in designing a finite wing because it constitutes a large part of the total drag. The induced drag is interpreted as caused by three physical phenomena. First the wing-tip vortices simply alter the flow field in a fashion to change the surface pressure distribution in the direction of increasing drag. The second is that the lift vector is tilted back, which results in increase of drag force because of the downward canted local wind about the wing. The last is the lost kinetic energy to generate the wing-tip vortices. It is well known that elliptical lift distribution gives the minimum induced drag (for example, see [1]). On the other hand, the parabolic lift distribution is known to give the minimum induced drag when the structural constraint is considered [2].

Reduction of the wave drag is also critical for a successful transonic wing design. The shock waves themselves result in an increase in drag. But in addition, the sharp pressure increase across the shock waves causes the flow to separate from the surface. Such flow separation can create substantial increase in drag. Thus, the last design goal is not to have any significant shock waves.

Unfortunately, drag minimization for itself is no goal for a wing design. There are considerable number of tradeoffs. One of the main tradeoffs is between drag and wing structure weight. An increase in the wing thickness allows the same bending moment to be carried with reduced skin thickness with an accompanying reduction in weight. On the other hand, it will lead to an increase in wave drag. There is also a tradeoff between drag and lift because induced drag increases in proportion to the square of the lift. For instance, a wing that achieves no induced drag would have no lift.

Therefore, the objectives of an aerodynamic wing optimization can typically characterized as minimization of each components of the total drag with constraints to maintain the required lift and the wing thickness, or maximization of lift-to-drag ratio *L/D* with constraints on the wing thickness.

4.3 Formulation of Optimization Problem

The objective of the present wing design problem is maximization of *L/D* at the transonic cruise design point, maintaining the minimum wing thickness required to stand the bending moment due to the lift distribution. The cruising Mach number and the angle of attack are set to 0.8 and 0 degree, respectively. The aerodynamic performance *L/D* is evaluated by the Navier-Stokes code that will be described in Sec. 4.4 on the assumption that the Reynolds number based on the root chord is 10^7.

In the present optimization, the planform of the supercritical wing in the NASA Energy Efficient Transport (EET) Program [3] was selected as the test configuration for the following design cases (Fig.4.1). Wing profiles of design candidates are generated by the PARSEC airfoils. The PARSEC parameters and the section angle of attack (in other words, root incident angle and twist angle) are given at seven span sections, of which spanwise locations are also treated as design variables except for the wing root and tip locations. The PARSEC parameters are rearranged from root to tip according to the airfoil thickness so that the resulting wings always have maximum thickness at the wing root. The twist angle parameter is also rearranged into numerical order from tip to root. The wing surface is then interpolated in spanwise direction by using the second-order Spline interpolation (Fig. 4.2). In total, 87 parameters determine a wing geometry. Parameter ranges of the design space are shown in Table 4.1. It should be noted that in ARGAs, user-defined design space is used just for the distribution of the initial population. ARGA can promote the search space outside of the user-defined design space even if it is ill defined.

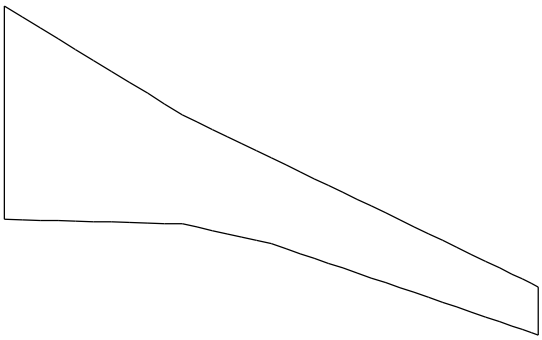

Fig.4.1 Wing planform

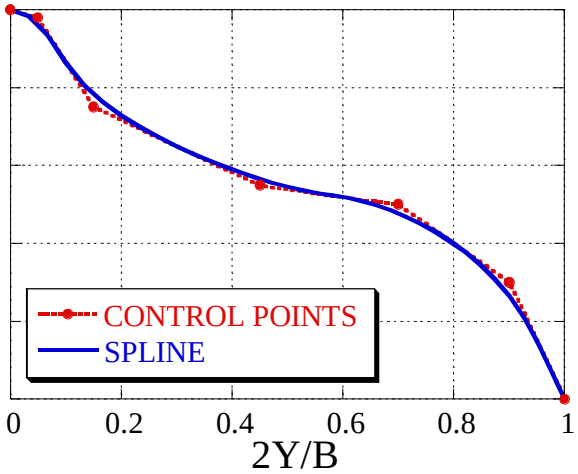

Fig. 4.2 Spline interpolation

Table 4.1 Parameter ranges of the design space

parameters	r_{LE}	Z_{TE}	α_{TE}	β_{TE}	X_{UP}	Z_{UP}	Z_{XXUP}	X_{LO}	Z_{LO}	Z_{XXLO}	twist

											angle
upper-bound	0.030	0.01	-3.00	8.00	0.70	0.18	0.00	0.60	0.02	0.90	7 degs.
lower-bound	0.002	-0.01	-13.00	4.00	0.30	0.08	-0.30	0.20	-0.04	0.30	-1 degs.

4.4 CFD Analysis for Aerodynamic Design

The flow physics can be represented by a wide range of approximations. Among them, the Reynolds-averaged Navier-Stokes equations provide the state-of-aft of aerodynamic performance evaluation. Although a Navier-Stokes calculation requires large computer resources to estimate wing performances within a reasonable time, the three-dimensional Navier-Stokes equations must be solved because flows around a wing involve significant viscous effects, such as potential boundary-layer separations and shock wave/boundary layer interactions in the transonic regime. In this chapter, a three-dimensional thin-layer Reynolds-averaged Navier-Stokes solver will be used to guarantee an accurate model of the flow field to demonstrate the feasibility of EA methodology. This code employs total variation diminishing type upwind differencing, the lower-upper symmetric Gauss-Seidel scheme, and the multigrid method. In the following subsections, details of the present code will be shown.

4.4.1 Symbols

$\hat{Q}$	generalized-coordinate conserved variables
$\hat{E},\hat{F},\hat{G}$	generalized-coordinate inviscid fluxes
$\hat{E}_v,\hat{F}_v,\hat{G}_v$	generalized-coordinate viscous fluxes
$\hat{S}$	generalized-coordinate viscous thin-layer fluxes
t,t	time
x,h,V	generalized curvilinear coordinates
r	density
u,v,w	vector components of velocity
U,V,W	contravariant velocity components
p	pressure
e	internal energy per unit mass
T	temperature
m	viscous coefficient
g	ratio of specific heats
Re	Reynolds number
c	speed of sound
NN	total number of grid points
A,B,C	inviscid flux Jacobian matrices
Δt	time step size
$r(A)$	spectral radius of A
R	right eigenvector matrix
Λ	eigenvalue matrix
L	left eigenvector matrix
I	identity matrix
Subscripts:	
∞	free-stream values
j,k	indices of grid point
R	the right state of cell interface
L	the left state of cell interface
Superscripts:	
$\pm$	splitting due to the sign of eigenvalues
n	time level

4.4.2 Governing Equations

The three-dimensional, compressible, thin layer Navier-Stokes equations are used to evaluate aerodynamic performance of a three-dimensional wing. Under a generalized curvilinear coordinate system (x,h,z), the Navier-Stokes equations are written in the strong conservation law form as

$$\frac{\partial \hat{Q}}{\partial t}+\frac{\partial \hat{E}}{\partial x}+\frac{\partial \hat{F}}{\partial h}+\frac{\partial \hat{G}}{\partial z}=\mathrm{Re}^{-1}\left(\frac{\partial \hat{E}_v}{\partial x}+\frac{\partial \hat{F}_v}{\partial h}+\frac{\partial \hat{G}_v}{\partial z}\right) \tag{4.1}$$

where

$$\hat{Q}=J^{-1}\begin{pmatrix} r \\ ru \\ rv \\ rw \\ e \end{pmatrix},\quad \hat{E}=J^{-1}\begin{pmatrix} rU \\ ruU+x_x p \\ rvU+x_y p \\ rwU+x_z p \\ U(e+p)-x_t p \end{pmatrix},\quad \hat{F}=J^{-1}\begin{pmatrix} rV \\ ruV+h_x p \\ rvV+h_y p \\ rwV+h_z p \\ V(e+p)-h_t p \end{pmatrix}$$

$$\hat{G}=J^{-1}\begin{pmatrix} rW \\ ruW+z_x p \\ rvW+z_y p \\ rwW+z_z p \\ W(e+p)-z_t p \end{pmatrix},\quad \hat{E}_v=J^{-1}\begin{pmatrix} 0 \\ x_x t_{xx}+x_y t_{xy}+x_z t_{xz} \\ x_x t_{yx}+x_y t_{yy}+x_z t_{yz} \\ x_x t_{zx}+x_y t_{zy}+x_z t_{zz} \\ x_x f_5+x_y g_5+x_z h_5 \end{pmatrix}$$

$$\hat{F}_v=J^{-1}\begin{pmatrix} 0 \\ h_x t_{xx}+h_y t_{xy}+h_z t_{xz} \\ h_x t_{yx}+h_y t_{yy}+h_z t_{yz} \\ h_x t_{zx}+h_y t_{zy}+h_z t_{zz} \\ h_x f_5+h_y g_5+h_z h_5 \end{pmatrix},\quad \hat{G}_v=J^{-1}\begin{pmatrix} 0 \\ z_x t_{xx}+z_y t_{xy}+z_z t_{xz} \\ z_x t_{yx}+z_y t_{yy}+z_z t_{yz} \\ z_x t_{zx}+z_y t_{zy}+z_z t_{zz} \\ z_x f_5+z_y g_5+z_z h_5 \end{pmatrix}$$

$$f_5=t_{xx}u+t_{xy}v+t_{xz}w+mP_r^{-1}(g-1)^{-1}\partial_x c^2$$

$$g_5=t_{yx}u+t_{yy}v+t_{yz}w+mP_r^{-1}(g-1)^{-1}\partial_y c^2$$

$$h_5=t_{zx}u+t_{zy}v+t_{zz}w+mP_r^{-1}(g-1)^{-1}\partial_z c^2$$

with the stress terms,

$$t_{xx}=\tfrac{2}{3}m(2u_x-v_y-w_z),\ t_{yy}=\tfrac{2}{3}m(2v_y-w_z-u_x),$$

$$t_{zz}=\tfrac{2}{3}m(2w_z-u_x-v_y),$$

$$t_{xy}=t_{yx}=m(u_y+v_x),\ t_{yz}=t_{zy}=m(v_z+w_y),$$

$$t_{zx}=t_{xz}=m(w_x+u_z)$$

Metrics and Jacobian are given by

$$x_x=J(y_h z_z-y_z z_h),\ x_y=J(z_h x_z-z_z x_h),\ x_z=J(x_h y_z-x_z y_h),$$

$$h_x=J(y_z z_x-y_x z_z),\ h_y=J(z_z x_x-z_x x_z),\ h_z=J(x_z y_x-x_x y_z)?$$

$$z_x=J(y_x z_h-y_h z_x),\ z_y=J(z_x x_h-z_h x_x),\ z_z=J(x_x y_h-x_h y_x)$$

$$J^{-1}=x_x y_h z_z+y_x z_h x_z+z_x x_h y_z-x_x z_h y_z-y_x x_h z_z-z_x y_h x_z$$

The contravariant velocity components are defined as

$$U=x_t+x_x u+x_y v+x_z w$$

$$V=h_t+h_x u+h_y v+h_z w$$

$$W = \xi_t + \xi_x u + \xi_y v + \xi_z w$$

Pressure is related to the conservative variables Q by the equation of state

$$p = (\gamma - 1)\left\{ e - \frac{1}{2}\rho (u^2 + v^2 + w^2) \right\} \tag{4.2}$$

In high Reynolds number flows, the effects of viscosity are concentrated near wall boundaries and in wake regions. Considering the memory and CPU time requirement, enough grid points are usually available only near the wall surfaces. Hence, the resulting grid has fine grid spacing normal to the surface and coarse grid spacing along the surface.

Even when the full Navier-Stokes equations are discretized, the viscous terms associated with derivatives along the body will not be resolved and in most cases for attached and mildly separated flows these terms are negligible. Only the terms normal to the body will be resolved by sufficiently fine grid spacing and these are the substantial terms.

Therefore, the following thin layer Navier-Stokes equations have been widely used for a variety of applications.

$$\frac{\partial \hat{Q}}{\partial t} + \frac{\partial \hat{E}}{\partial \xi} + \frac{\partial \hat{F}}{\partial \eta} + \frac{\partial \hat{G}}{\partial \zeta} = \mathrm{Re}^{-1} \frac{\partial \hat{S}}{\partial \zeta} \ , \ \hat{S} = \hat{G}_v \tag{4.3}$$

The thin layer approximation may break down for low Reynolds numbers and in regions of massive flow separation.

4.4.3 Numerical Algorithm

Following Warming and Beam[4], an implicit three-point time differencing scheme can be written as

$$\Delta \hat{Q}^n = \frac{J\Delta t}{1+j} \frac{\partial}{\partial t}\left(\Delta \hat{Q}^n\right) + \frac{\Delta t}{1+j} \frac{\partial}{\partial t} \hat{Q}^n + \frac{j}{1+j} \Delta \hat{Q}^{n-1} + O\left[\left(J - \frac{1}{2} - j \right) \Delta t^2 + \Delta t^3 \right] \tag{4.4}$$

where $\Delta \hat{Q}^n = \hat{Q}^{n+1} - \hat{Q}^n$ and $\Delta \hat{Q}^n = \hat{Q}(n\Delta t)$. For the first-order scheme in time the parameters J and j become 1 and 0, respectively. Applying Eq.(4.4) to Eq. (4.3) , one obtains

$$\hat{Q}^{n+1} - \hat{Q}^n + h(\hat{E}_x^{n+1} + \hat{F}_h^{n+1} + \hat{G}_z^{n+1} - Re^{-1} \hat{S}_z^{n+1}) = 0 \tag{4.5}$$

where $h = \Delta t$.

Using Eq.(4.5), $\hat{Q}^{n+1}$ can be obtained from given $\hat{Q}^n$. The flux vectors $\hat{E}$, $\hat{F}$, $\hat{G}$ and $\hat{S}$ are nonlinear functions of $\hat{Q}$ and therefore Eq. (4.5) is nonlinear in $\hat{Q}^{n+1}$. The nonlinear terms are linearized in time about $\hat{Q}^n$ by a Taylor expansion such that

$$\begin{aligned}
\hat{E}^{n+1} &= \hat{E}^n + \hat{A}^n \Delta \hat{Q}^n + O(h^2) \\
\hat{F}^{n+1} &= \hat{F}^n + \hat{B}^n \Delta \hat{Q}^n + O(h^2) \\
\hat{G}^{n+1} &= \hat{G}^n + \hat{C}^n \Delta \hat{Q}^n + O(h^2) \\
Re^{-1} \hat{S}^{n+1} &= Re^{-1}\left(\hat{S}^n + J^{-1} \hat{M}^n \Delta \hat{Q}^n\right) + O(h^2)
\end{aligned} \tag{4.6}$$

where $\hat{A} = \partial \hat{E} / \partial \hat{Q}$, $\hat{B} = \partial \hat{F} / \partial \hat{Q}$, $\hat{C} = \partial \hat{G} / \partial \hat{Q}$ and $\hat{M} = \partial \hat{S} / \partial \hat{Q}$ are the flux Jacobians and $\Delta \hat{Q}^n$ is $O(h)$.

Applying Eq. (4.6) to Eq. (4.5) and combining the $\Delta \hat{Q}^n$ terms produces the "delta form" of the algorithm, one obtains

$$\left[I + h\left(\partial_\xi \hat{A}^n + \partial_\eta \hat{B}^n + \partial_\zeta \hat{C}^n - Re^{-1} J^{-1} \partial_\zeta \hat{M} \right) \right] \Delta \hat{Q}^n = -h\left(\partial_\xi \hat{E}^n + \partial_\eta \hat{B}^n + \partial_V \hat{C}^n - \mathrm{Re}^{-1} J^{-1} \partial_V \hat{S}^n \right) \tag{4.7}$$

The left and right hand side of Eq. (4.7) are called as the "implicit" and "explicit" parts of the algorithm, respectively.

4.4.3.1 LU-SGS Method

The LU-SGS (lower-upper symmetric Gauss-Seidel) algorithm is efficient and robust implicit relaxation scheme originally suggested by Yoon [5]. A slightly modified form of the LU-SGS method [6] is given by

$$\begin{aligned}&\left[h\left(\hat{A}^{+}\Delta\bar{Q}\right)_{i-1,j,k}+h\left(\hat{B}^{+}\Delta\bar{Q}\right)_{i,j-1,k}+h\left(\hat{C}^{+}\Delta\bar{Q}\right)_{i,j,k-1}\right]\\&+\left[I+h\hat{A}^{+}-h\hat{A}^{-}+h\hat{B}^{+}-h\hat{B}^{-}+h\hat{C}^{+}-h\hat{C}^{-}+\frac{m}{\mathrm{Re}\cdot r}|\nabla z|^{2}I\right]\Delta\hat{Q}_{i,j,k}\\&+\left[h\left(\hat{A}^{-}\Delta\bar{Q}\right)_{i+1,j,k}+h\left(\hat{B}^{-}\Delta\bar{Q}\right)_{i,j+1,k}+h\left(\hat{C}^{-}\Delta\bar{Q}\right)_{i,j,k+1}\right]=RHS\end{aligned} \tag{4.8a}$$

where

$$\begin{aligned}\hat{A}^{\pm}&=\frac{s_x^{\pm}}{2}\left\{\hat{A}\pm r(\hat{A})I\right\}\pm\frac{(c-1)}{2}r(\hat{A})I\,,\\\hat{B}^{\pm}&=\frac{s_h^{\pm}}{2}\left\{\hat{B}\pm r(\hat{B})I\right\}\pm\frac{(c-1)}{2}r(\hat{B})I\\\hat{C}^{\pm}&=\frac{s_z^{\pm}}{2}\left\{\hat{C}\pm r(\hat{C})I\right\}\pm\frac{(c-1)}{2}r(\hat{C})I\pm\frac{m}{Re\cdot r}|\nabla z|^{2}I\end{aligned} \tag{4.8b}$$

$$s_k=\begin{cases}1, & if \quad \pm\left[(k_t+k_xu+k_yv+k_zw)\pm c\sqrt{k_x^2+k_y^2+k_z^2}\right]\geq 0\\0, & if \quad \pm\left[(k_t+k_xu+k_yv+k_zw)\pm c\sqrt{k_x^2+k_y^2+k_z^2}\right]<0\end{cases} \tag{4.9}$$

where $k=x,h,v$ and $c=1.01$ typically. $\hat{A}^{\pm}$ $\hat{B}^{\pm}$ and $\hat{C}^{\pm}$ are constructed so that the eigenvalues of "+" matrices are nonnegative and those of "-" matrices are nonpositive. By Eq. (4.8b), the present numerical method eliminates the need for block diagonal inversions. Note that this is a two-factored scheme so that the algorithm can be written as

Forward sweep :

$$\begin{aligned}\Delta\bar{Q}'_{i,j,k}=&\left[RHS_{i,j,k}+h\left(\hat{A}^{+}\Delta\bar{Q}'\right)_{i-1,j,k}+h\left(\hat{B}^{+}\Delta\bar{Q}'\right)_{i,j-1,k}+h\left(\hat{C}^{+}\Delta\bar{Q}'\right)_{i,j,k-1}\right]\\&\Big/\left(1+hcr(\hat{A})+hcr(\hat{B})+hcr(\hat{C})+2\frac{m+m_t}{Re\cdot r}|\nabla z|^{2}I\right)_{i,j,k}\end{aligned} \tag{4.10}$$

Backward sweep :

$$\begin{aligned}\Delta\bar{Q}_{i,j,k}=&\Delta\bar{Q}'_{i,j,k}-\left[h\left(\hat{A}^{-}\Delta\bar{Q}'\right)_{i+1,j,k}+h\left(\hat{B}^{-}\Delta\bar{Q}'\right)_{i,j+1,k}+h\left(\hat{C}^{-}\Delta\bar{Q}'\right)_{i,j,k+1}\right]\\&\Big/\left(1+hcr(\hat{A})+hcr(\hat{B})+hcr(\hat{C})+2\frac{m+m_t}{Re\cdot r}|\nabla z|^{2}I\right)_{i,j,k}\end{aligned} \tag{4.11}$$

Though this scheme requires no block-matrix inversion, it introduces large dissipation through the time integration. Only when the solution converges to a steady state, its effect banishes. Although the LU-SGS method is first-order accurate in time similar to other implicit methods, unsteady calculations have to be carried out carefully with the LU-SGS method. The use of Newton iteration [7,8] will be beneficial not only for removing the excess dissipation but also for obtaining the second-order accuracy in time.

4.4.3.2 HLLEW Scheme

The cell-vertex finite-volume method are applied to the explicit part of Eq. (4.7) to

approximate the differential operators ∂_x ∂_h and ∂_z as

$$\boldsymbol{RHS} \cong -\boldsymbol{h}\left[\hat{\boldsymbol{E}}_{i+\frac{1}{2}}{}^{n} - \hat{\boldsymbol{E}}_{i-\frac{1}{2}}{}^{n} + \hat{\boldsymbol{F}}_{j+\frac{1}{2}}{}^{n} - \hat{\boldsymbol{F}}_{j-\frac{1}{2}}{}^{n} + \hat{\boldsymbol{G}}_{k+\frac{1}{2}}{}^{n} - \hat{\boldsymbol{G}}_{k-\frac{1}{2}}{}^{n} - \boldsymbol{Re}^{-1}\boldsymbol{J}^{-1}(\hat{\boldsymbol{S}}_{k+\frac{1}{2}}{}^{n} - \hat{\boldsymbol{S}}_{k-\frac{1}{2}}{}^{n})\right] \quad (4.12)$$

The cell interface flux is evaluated by the HLLEW (Harten-Lax-van Leer-Einfeldt-Wada) method [9] as

$$\hat{\boldsymbol{E}}_{i+\frac{1}{2}} = \frac{1}{2}\left[\hat{\boldsymbol{E}}_L + \hat{\boldsymbol{E}}_R - \hat{\bar{\boldsymbol{R}}}\tilde{\Lambda}\hat{\bar{\boldsymbol{L}}}(\hat{\boldsymbol{Q}}_R - \hat{\boldsymbol{Q}}_L)\right] \quad (4.13)$$

where

$$\tilde{\Lambda} = \frac{\boldsymbol{b}_R^+ + \boldsymbol{b}_L^-}{\boldsymbol{b}_R^+ - \boldsymbol{b}_L^-}\bar{\Lambda} - 2\frac{\boldsymbol{b}_R^+\boldsymbol{b}_L^-}{\boldsymbol{b}_R^+ - \boldsymbol{b}_L^-}\boldsymbol{I} + \Lambda'$$

$$\bar{\Lambda} = \mathrm{Diag}\left[\bar{\boldsymbol{U}}, \bar{\boldsymbol{U}}, \bar{\boldsymbol{U}}, \bar{\boldsymbol{U}} + \bar{\boldsymbol{c}}\sqrt{x_x^2 + x_y^2 + x_z^2}, \bar{\boldsymbol{U}} - \bar{\boldsymbol{c}}\sqrt{x_x^2 + x_y^2 + x_z^2}\right]$$

$$\Lambda' = \mathrm{Diag}\left[-2\,d\min(\boldsymbol{b}_R^+, \boldsymbol{b}_L^-), -2\,d\min(\boldsymbol{b}_R^+, \boldsymbol{b}_L^-), -2\,d\min(\boldsymbol{b}_R^+, \boldsymbol{b}_L^-), 0, 0\right]$$

$$d = \min\left(\frac{r_{LR}}{|s_1|}, \frac{1}{2}\right)$$

$$s_1 = \Delta r - \Delta \boldsymbol{p}/\bar{\boldsymbol{c}}^2$$

The overbar indicates Roe-averaged quantities. This scheme satisfies all the stability, entropy, and positively conservative conditions required for the nonlinear difference equations.

The HLLE scheme approximates the solution of the Riemann problem with two waves propagating with speed

$$\boldsymbol{b}_R = \max\left(\bar{\boldsymbol{U}} + \bar{\boldsymbol{c}}\sqrt{x_x^2 + x_y^2 + x_z^2}, \boldsymbol{U}_R + \boldsymbol{c}_R\sqrt{x_x^2 + x_y^2 + x_z^2}, 0\right)$$

and

$$\boldsymbol{b}_L = \min\left(\bar{\boldsymbol{U}} - \bar{\boldsymbol{c}}\sqrt{x_x^2 + x_y^2 + x_z^2}, \boldsymbol{U}_L - \boldsymbol{c}_L\sqrt{x_x^2 + x_y^2 + x_z^2}, 0\right)$$

and a state Q_{LR} between those waves. Compared with the Roe scheme, the HLLE scheme introduces large numerical dissipation at contact discontinuities. The HLLEW scheme improves the resolution at contact discontinuities by adding Λ'. The resulting scheme reduces to the Roe scheme when d=1/2 and to the HLLE scheme when d=0. Because s_1 represents a jump in entropy, it is zero for isentropic flows. Then, the present scheme results in the Roe scheme. As the jump in entropy becomes large, the present scheme turns into the HLLE scheme.

4.4.3.3 Modified Differentiable Limiter

Higher-order numerical fluxes are obtained from higher order interpolation of the primitive variables for the left and right states at the cell interface [10] as

$$\boldsymbol{V}_{Li+1/2} = \left[1 + \frac{f}{4}\{(1-k)\nabla + (1+k)\Delta\}\right]\boldsymbol{V}_i$$

$$\boldsymbol{V}_{Ri+1/2} = \left[1 - \frac{f}{4}\{(1+k)\nabla + (1-k)\Delta\}\right]\boldsymbol{V}_{i+1} \quad (4.14)$$

where V is the primitive flow variables. ∇ and Δ are backward and forward difference operations,

respectively. Third-order interpolation is obtained from k=1/3. The limiter function f in [11] and [12] is given as

$$f(\boldsymbol{V}_i) = \frac{3\nabla \boldsymbol{V}_i \cdot \Delta \boldsymbol{V}_i + e_i^2}{2(\Delta \boldsymbol{V}_i - \nabla \boldsymbol{V}_i)^2 + 3\nabla \boldsymbol{V}_i \cdot \Delta \boldsymbol{V}_i + e_i^2} \tag{4.15}$$

In this paper, e_i^2 is given by

$$e_i^2 = \max\left(24.0\left|\nabla x\right|_i^{-3}, 10^{-12}\right) \tag{4.16}$$

4.4.3.4 Turbulence Model

Nondimensional viscous coefficient is given by a sum of laminar and turbulent viscosities as

$$\frac{\mu}{\mu_\infty} = \frac{\mu_l}{\mu_\infty} + \frac{\mu_t}{\mu_\infty} \tag{4.17}$$

Laminar viscosity μ_l is defined by using Sutherland's formula as

$$\frac{\mu_l}{\mu_\infty} = \left(\frac{\boldsymbol{T}}{\boldsymbol{T}_\infty}\right)^{\frac{3}{2}}\left(\frac{\boldsymbol{T}_\infty + \boldsymbol{T}_0}{\boldsymbol{T} + \boldsymbol{T}_0}\right), \quad \boldsymbol{T}_0 = 110\boldsymbol{K} \tag{4.18}$$

Turbulent viscosity μ_t is calculated by an algebraic mixing length model by Baldwin-Lomax [13]. The inner layer is governed by the Prandtl mixing length with Van Driest damping, and the outer layer follows the Caluser approximation. Computed vorticity is used in defining the reference mixing length required for the outer layer. The turbulence model was designed specifically for use with the thin layer approximation. The model is appropriate to attached and mildly separated boundary layers.

Turbulent viscosity can be written as

$$\mu_t = \begin{cases} \mu_{tinner} = \rho \boldsymbol{l}^2 |\omega| & \boldsymbol{y} \le \boldsymbol{y}_{crossover} \\ \mu_{touter} = \boldsymbol{K}\boldsymbol{C}_{CP}\,\rho \boldsymbol{F}_{WAKE}\boldsymbol{F}_{KLEB}(\boldsymbol{y}) & \boldsymbol{y}_{crossover} \le \boldsymbol{y} \end{cases} \tag{4.19}$$

where

$$\boldsymbol{l} = \boldsymbol{k}\boldsymbol{y}\left[1 - \exp(-\boldsymbol{y}^+ / \boldsymbol{A}^+)\right],\ \boldsymbol{y}^+ = \frac{\sqrt{\rho_w \tau_w}\,\boldsymbol{y}}{\mu_w},$$

$$|\omega| = \sqrt{\left(\frac{\partial \boldsymbol{u}}{\partial \boldsymbol{y}} - \frac{\partial \boldsymbol{v}}{\partial \boldsymbol{x}}\right)^2 + \left(\frac{\partial \boldsymbol{v}}{\partial \boldsymbol{z}} - \frac{\partial \boldsymbol{w}}{\partial \boldsymbol{y}}\right)^2 + \left(\frac{\partial \boldsymbol{w}}{\partial \boldsymbol{x}} - \frac{\partial \boldsymbol{u}}{\partial \boldsymbol{z}}\right)^2}$$

$$\boldsymbol{F}_{WAKE} = \min\left(\boldsymbol{y}_{\max}\boldsymbol{F}_{\max}, \boldsymbol{C}_{WK}\boldsymbol{y}_{\max}\boldsymbol{u}_{diff}^2 / \boldsymbol{F}_{\max}\right)$$

$$\boldsymbol{F}_{KLEB}(\boldsymbol{y}) = \left[1 + 5.5\left(\frac{\boldsymbol{C}_{KLEB}\boldsymbol{y}}{\boldsymbol{y}_{\max}}\right)^6\right]^{-1}$$

$$\boldsymbol{u}_{diff} = \left(\sqrt{\boldsymbol{u}^2 + \boldsymbol{v}^2 + \boldsymbol{w}^2}\right)_{\max} - \left(\sqrt{\boldsymbol{u}^2 + \boldsymbol{v}^2 + \boldsymbol{w}^2}\right)_{\min}$$

y is the distance from wall and $y_{crossover}$ is the minimum distance satisfying $\mu_{tinner} \ge \mu_{touter}$. F_{max} is the maximum value of the following function

$$\boldsymbol{F}(\boldsymbol{y}) = \boldsymbol{y}|\omega|\left[1 - \exp\left(-\boldsymbol{y}^+ / \boldsymbol{A}^+\right)\right] \tag{4.20}$$

and y_{max} is a distance from wall to F_{max} location. The above coefficients are defined as

$$\boldsymbol{A}^+ = 26,\ \boldsymbol{k} = 0.4,\ \boldsymbol{C}_{CP} = 1.6,\ \boldsymbol{C}_{KLEB} = 0.3,\ \boldsymbol{C}_{WK} = 1.0,$$

$$\boldsymbol{K} = 0.0168$$

4.4.3.5 Time Stepping Technique

In the following calculations, a locally varying time step [14] was taken as

$$\Delta t_{i,j,k} = \Delta t_{global} \frac{1}{1+\sqrt{\left(J^{-1}\right)_{rms} J_{i,j,k}}} \tag{4.21}$$

where

$$\left(J^{-1}\right)_{rms} = \left(\frac{1}{NN} \sum_{i,j,k} \left(J^{-1}_{i,j,k}\right)^2 \right)^{\frac{1}{2}} \tag{4.22}$$

NN is a total number of grid points. This expression reduces the effective time step in regions of clustered grid while a large time step is maintained in the inviscid regions. Local time-stepping is useful for three-dimensional computations where high mesh refinement in two or more coordinate directions is required.

4.4.3.6 Multigrid Method

Multigrid techniques have derived from the observation that many numerical methods for solving discretized partial differential equations are adept at smoothing high frequency error components, but are a poor smoother for lower frequency components. Convergence histories at first show a region of rapid error reduction by removing high frequency components. However, a long region of slow error reduction corresponding to the slow expulsion of the low frequency modes follows.

The multigrid method efficiently dissipates the lower frequency errors using a sequence of grids G_h ,G_{2h} ,G_{4h} , ... where G_h denotes the finest grid from which successively coarser grids can be formed by deleting every other grid line in all coordinate directions. On coarser grids, the fine-grid low frequency error components are resolved as higher frequencies due to the increased grid spacing, and thus they are effectively damped. When this correction is interpolated back to the fine grid, high frequency errors can be generated but they are damped quickly by the fine-grid smoothing iteration. A sequence of grids about a NACA0012 airfoil is shown in Fig. 4.3.

The multigrid method used in the current study is the full approximation scheme (FAS) [15]. The current cycling strategy uses a V-cycle with three grid levels as shown in Fig 4.4. On the coarser grids, two time steps are proceeded. Convergence was not improved significantly any more by increasing the grid levels in the V-cycle or by changing the V-cycle to the W-cycle.

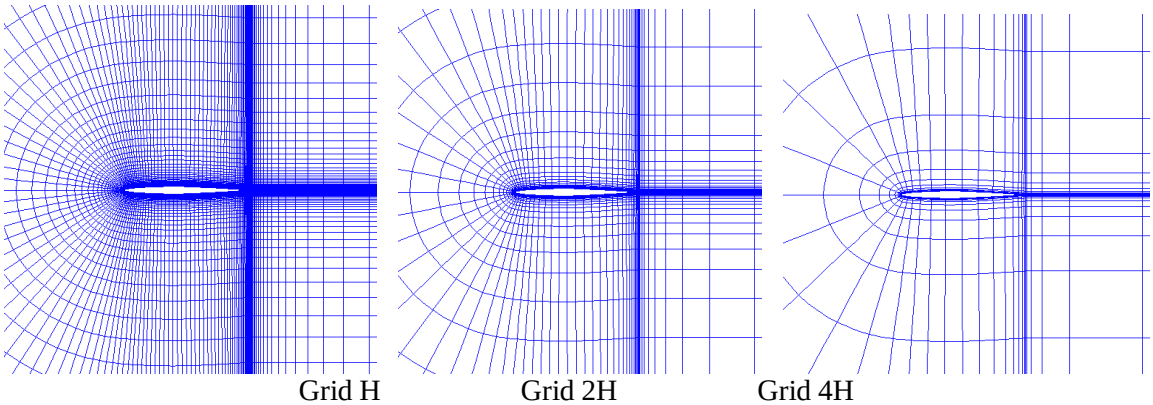

Grid H Grid 2H Grid 4H

Figure 4.3 Grid sequence

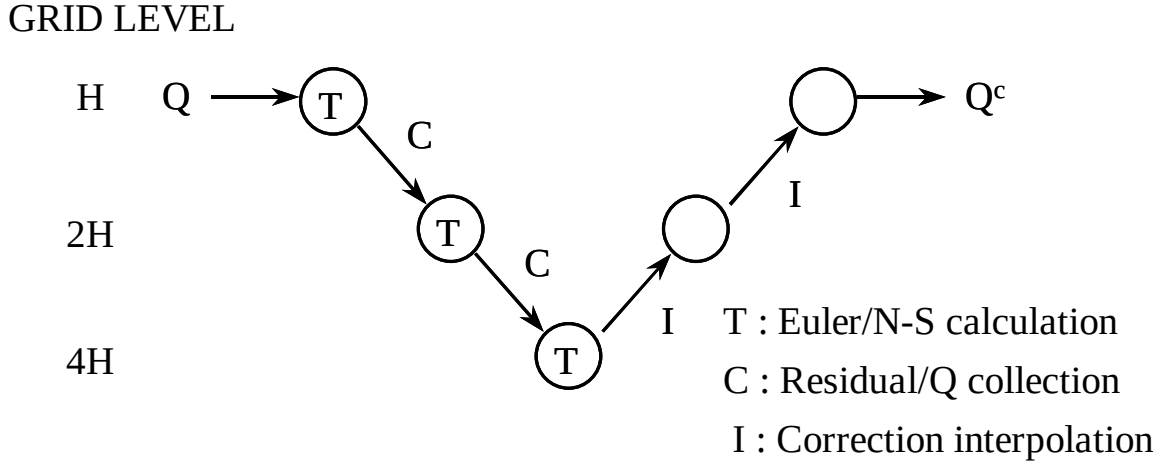

Figure 4.4 V-cycle

The multigrid method is illustrated by a grid sequence between two grid levels. The Euler or Navier-Stokes equations are solved approximately on a fine grid H by dividing the domain into discrete cells yielding a system of algebraic equations as

$$M\Delta Q_H = -\Delta t L_H(Q_H) = -\Delta t R_H \tag{4.23}$$

where M is the explicit or implicit relaxation operator of the scheme considered and $L_H(Q_H)$ is the explicit part of Eq. (4.7), corresponding to the current conservative variables Q_H. After Eq. (4.23) is calculated, the residual and the dependent variables on the first coarse grid are calculated by restricting the corresponding fine-grid values as

$$Q_{2H} = I_H^{2H} Q_H \tag{4.24}$$

$$R_{2H} = I_H^{2H} R_H \tag{4.25}$$

A volume weighted restriction operator I_H^{2H} transfers values on the fine grid H to the coarse grid 2H as

$$I_H^{2H} Q_H = \sum VQ / \sum V \tag{4.26}$$

$$I_H^{2H} R_H = \sum VR / \sum V \tag{4.27}$$

where the summations are taken over the entire fine grid cells which make up the coarse grid cell and V is volume of the fine-grid cell. This restriction operator is conservative and thus the surface integral of the fluxes crossing the cell boundaries on the coarse grid are the same as the corresponding integral on the fine grid. The relative truncation error on the coarse grid is calculated from the

$$t_{2H} = L_{2H}(I_H^{2H} Q_H) - I_H^{2H} R_H \tag{4.28}$$

On the coarse grid, a few iterations of the approximate factorization scheme can be conducted by adding the relative truncation error as

$$M\Delta Q_{2H} = -\Delta t L_{2H}(Q_{2H} - t_{2H}) = -\Delta t R_{2H} \tag{4.29}$$

Since t_{2H} has been previously calculated, the residual is easily calculated by simply calculating $L_{2h}(Q_{2h}^c)$ from the most current values on the mesh and subtracting t_{2h}. The residual on the coarser grid is thus expressed as

$$R_{2H} = L_{2H}(Q_{2H}) - t_{2H} \tag{4.30}$$

The correction V_{2H} is calculated as

$$V_{2H} = Q_{2H} - I_H^{2H} Q_H \tag{4.31}$$

This correction is transferred to the fine grid by using trilinear interpolation I_H^{2H}.

$$Q_H^c = Q_H + I_{2H}^H V_{2H} \tag{4.32}$$

The fine-grid solution is fully updated by one more smoothing iteration using Eq. (4.23).

Compared with the conventional time-marching scheme, the V-cycle requires additional computations on coarser grids. However, on the first coarse grid 2H, the computational efforts are reduced to 1/8 of the calculation on the finest grid in the three dimensions since the number of nodes is reduced to 1/2 in each coordinate direction. Thus the computational cost on coarser grids is extremely small. Similarly, it becomes 1/64 on the 4H grid. Thus the total computational cost of the present V-cycle becomes,

$$2+2/8+2/64? \; 2.3 \tag{4.33}$$

while 6 time steps are computed in one cycle.

Another merit of multigrid strategy is that the time step sizes limited by the CFL number can be doubled as the grid spacing is doubled from the previous grid. Then the multigrid cycle proceeds the total time step sizes of

$$2\times(\Delta t) + 2\times(2\Delta t) + 2\times(4\Delta t) = 13\Delta t \tag{4.34}$$

compared with $6\,\Delta t$ for the single grid method, where Δt represents the time step size on the fine grid.

4.5 Estimation of Required Thickness

To estimate the required thickness distribution to stand the bending moment due to the lift distribution, the wing is modeled by a thin walled box-beam as shown in Fig. 4.5.

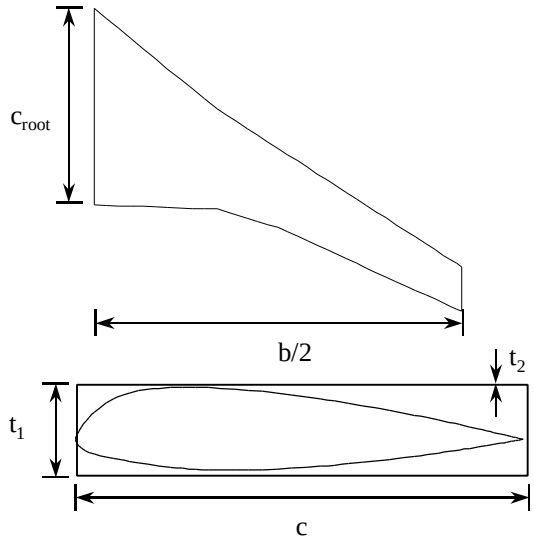

Fig. 4.5 Wing planform geometry and cross section of the wing

The shear panels of the box-beam are considered to shear the bending moment. From the load *L*, the spanwise bending moment distribution *M* is calculated by

$$\frac{\boldsymbol{d}^2\boldsymbol{M}}{\boldsymbol{dy}^2} = -\boldsymbol{L} \tag{4.35}$$

For the brevity, the lift distribution is replaced by spanwise concentrated loads. The bending stress at each station is given by

$$\sigma = \frac{M}{I}\frac{t_1}{2} \tag{4.36}$$

where

$$I = 2 \cdot \left(\frac{t_1}{2}\right)^2 \cdot t_2 \cdot c = \frac{1}{2} t_1^2 \cdot c \cdot t_2 \tag{4.37}$$

The constraint is then given by the local stress to be less than the ultimate shear stress of, say, Aluminum alloy 2024-T351.

$$\sigma < \sigma_{ultimate} \tag{4.38}$$

Using Eqs. (4.36) to (4.38), we obtain the minimum thickness t_{min} at each segment,

$$t > \frac{M}{\sigma_{ultimate} \cdot c \cdot t_2} = t_{\min} \tag{4.39}$$

Following assumptions are made: the thickness of the skin panels are 2.5[cm] and its ultimate normal stress is 39[ksi]. The length of the chord at wing root C_{root} and maximum wingspan *b/2* are 10[m] and 18.8[m], respectively. (see, for example, [16]).

4.6 Optimization Using EA

The present EA is the real-coded ARGA described in Chap.2. Parameters of the ARGA, w_m, w_s and N, are set to 1, 0.3 and 4, respectively. The structured coding coupled with one-point crossover proposed in Chap. 3 is also incorporated. The present EA adopts the elitist strategy where the best and the second best individuals in each generation are transferred into the next generation without any crossover or mutation. The parental selection consists of the stochastic universal sampling and the ranking method using Michalewicz's nonlinear function. Mutation takes place at a probability of 10% and then adds a random disturbance to the corresponding gene in the amount up to $\pm$ 10% of each parameter range in Table 4.1. The population size is kept at 64 and the maximum number of generations is set to 65. The initial population is generated randomly over the entire design space.

The main concern related to the use of EAs coupled with three-dimensional Navier-Stokes solvers for aerodynamic shape designs is the required computational effort. In the present case, each CFD evaluation takes about 100 min. of CPU time even on a vector computer. Because the present optimization evaluates 64 x 65 = 4160 design candidates, sequential evolutions would take almost 7000 h (more than half a year!).

Fortunately, parallel vector computers are now available in many institutions and universities. In addition, EAs are intrinsically parallel algorithms and can be easily parallelized. One of such computers is *Numerical Wind Tunnel* (*NWT*)[17] located at National Aerospace Laboratory in Japan. NWT is a MIMD parallel computer with 166 vector-processing elements (PEs) and its total peak performance and the total main memory capacity are about 280 GFLOPS and 45GB, respectively. In the present optimization, evaluation process at each generation was parallelized using the master-slave concept; the grid generations and the flow calculations associated to the individuals of a generation were distributed into 64 PEs of NWT. This made the corresponding turnaround time almost 1/64 because the CPU time used for EA operators are negligible.

To handle the structural constraint with the single-objective EA, the constrained optimization problem was transformed into an unconstrained problem as

$$\textit{fitness function} = \begin{cases} 100 + L/D & \textit{if} \quad t \geq t_{\min} \\ (100 + L/D) \cdot \exp(t - t_{\min}) & \textit{otherwise} \end{cases} \tag{4.40}$$

where t and t_{min} are thickness and minimum thickness at the span station of the maximum local stress. The exponential term penalizes the infeasible solutions by reducing the fitness function value. Because some design candidates can have negative *L*/*D*, the summation of 100 and *L*/*D* is used.

4.7 Results

The optimization history of the present EA is shown in Fig. 4.6 in terms of L/D. During the initial phase of the optimization, some members had a strong shock wave or failed to satisfy the structural constraint. However they were weeded out from the population because of the resultant penalties to the fitness function. The final design has L/D of 18.91 satisfying the given structural constraint. Aerodynamic performances of the design are summarized in Table 4.2. Compared with a typical long-range transport aircraft, the present wing has smaller C_L. Although L/D is an important aircraft performance measure because the range of an aircraft depends on it, wing optimizations by maximizing L/D may result in a design that has too lower lift to fly. Therefore, another constraint on lift or multiobjective approach is required for a wing design optimization.

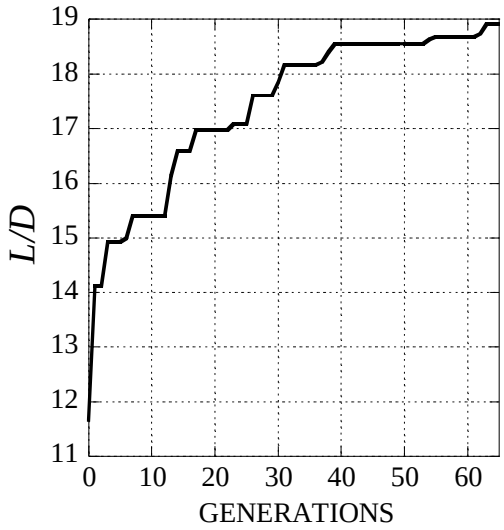

Fig. 4.6 Optimization history of L/D

Table 4.2 Aerodynamic performances of the design

C_L	0.26213
C_D	0.01386
L/D	18.9143

The wing thickness distribution of the design is given in Fig. 4.7. The minimum thickness constraint appears at the kink because the inboard sections of the wing have large chord lengths and allow a large moment. The design satisfies this structural constraint while minimizing its thickness distribution to reduce the wave drag.

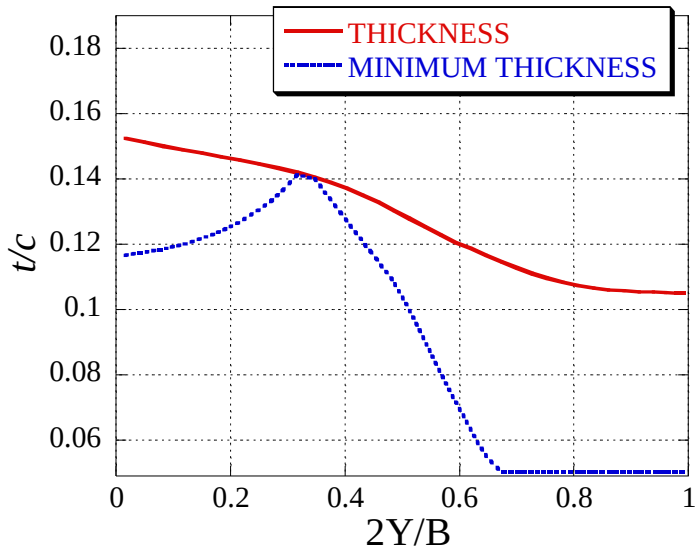

Fig. 4.7 Spanwise thickness distribution

Figure 4.8 compares the span load distribution of the designed wing with a parabola that is known to give the minimum induced drag when the structural constraint is considered. The design does not have the parabolic span load distribution but a straight load distribution, which helps to reduce the bending moment at the inboard of the wing. The thickness distribution for the corresponding parabolic span load distribution is presented in Fig. 4.9. This figure indicates that a design that minimizes the induced drag would have 18% thickness-to-chord. Such design would result in an unacceptably large wave drag associated with a stronger shock wave. The present structural constraint imposed a tradeoff between minimizations of induced drag and wave drag. The present straight span load distribution is a compromised design.

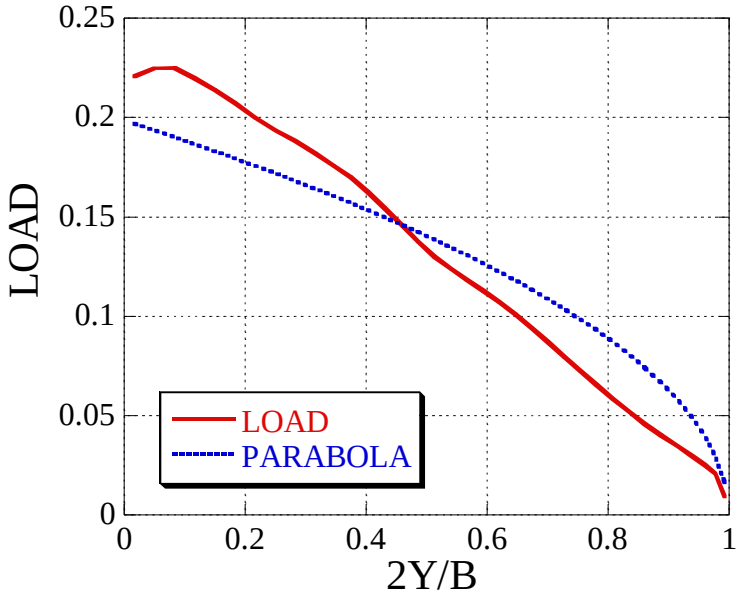

Fig. 4.8 Spanwise lift distribution

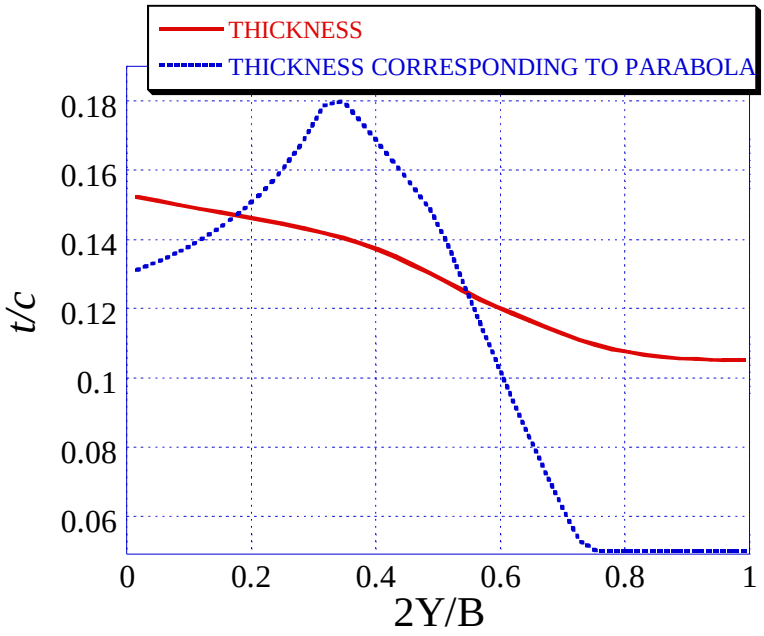

Fig. 4.9 Comparison of thickness distributions between the present design and the minimum induced-drag design

The spanwise twist angle distribution and its control points are illustrated in Fig. 4.10. The angle of attack drastically decreases at the kink. Because the inboard of the wing has large chord length it allows large bending moment and thus large twist angle. On the other hand, since the outboard has smaller chord length, the wing requires significant twisting down outside the kink to reduce the moment.

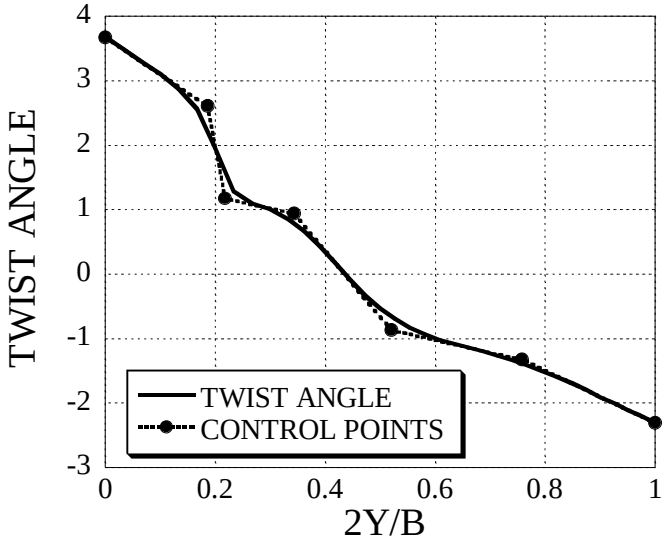

Fig. 4.10 Spanwise twist angle distribution

The designed airfoil sections and the corresponding pressure distributions at the 0, 33, and 66% spanwise locations are shown in Fig. 4.11. Neither any strong shock wave nor any flow separation are found that may significantly increase pressure drag.

4.8 Summary

The real-coded ARGA coupled with structured coding strategy has been applied to an

aerodynamic design optimization of a transonic wing shape for generic transport aircraft. Aerodynamic performances of the design candidates are evaluated by using the three-dimensional compressive Navier-Stokes equations. Structural constraint is introduced to avoid an apparent solution of zero thickness wing for low drag in high speeds.

To overcome enormous computational time necessary for the optimization, aerodynamic evaluations are distributed to the PEs of NWT. Parallelization of EA on NWT is straightforward, and its performance is extremely good in reducing the turnaround time.

The present structural constraint imposed a tradeoff between minimizations of induced drag and wave drag. The straight span load distribution of the design is a compromised design. The designed wing has a fully attached flow and the allowable minimum thickness so that pressure drag and wave drag are minimized under the present structural constraint. The present design ensures the feasibility of the present approach.

Because the tradeoff between minimizations of induced drag and wave drag directly related to the structural strength, more accurate structural modeling is desired. In addition, because the structural strength is a function of the structural weight, multiobjective optimization by an MOEA for minimizing both aerodynamic drag and structural weight is required.

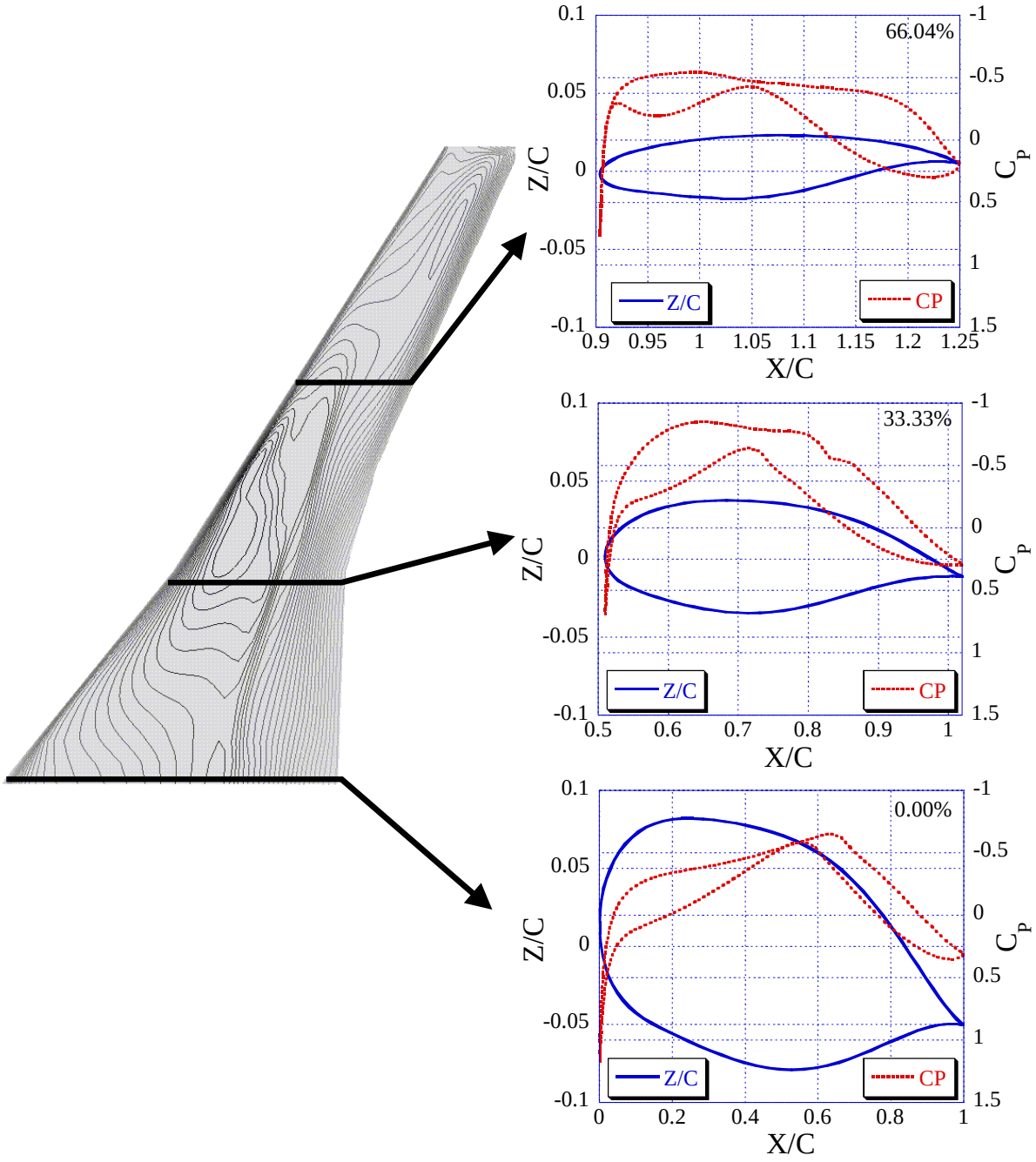

Fig. 4.11 Designed airfoil sections and the corresponding pressure distributions at the 0, 33, and 66% spanwise locations

References

[1] Stinton, D., *The Design of the Aeroplane*, Blackwell Scientific Publications, Ltd., Oxford, London, 1983, Chap. 4.

[2] Jones, R. T., *Wing Theory*, Princeton University Press, Princeton, NJ, 1990, Chap. 7.

[3] Jacobs, P. F., "Experimental Trim Drag Values and Flow-Field Measurements or a Wide-Body Transport Model with Conventional and Supercritical Wings," NASA TP 2071, 1982.

[4] Warming, R. F. and Beam, R., "On the Construction and Application of Implicit Factored Schemes for Conservation Laws," SIAM-AMS Proceedings, Vol. 1, 1978, pp.85-129.

[5] Yoon, S. and Jameson, A., "Lower-Upper Symmetric-Gauss-Seidel Method for the Euler and Navier-Stokes Equations," *AIAA Journal*, Vol. 26, Sep. 1988, pp.1025-1026.

[6] Obayashi, S. and Guruswamy, G. P., "Convergence Acceleration of an Aeroelastic Navier-Stokes Solver," *AIAA Journal*, Vol. 33, No. 6, 1995, pp.1134-1141.

[7] Chen, C. L., McCroskey, W. J. and Obayashi, S., "Numerical Solutions of Forward-Flight Rotor Flow Using an Upwind Method," *Journal of Aircraft*, Vol. 28, No. 6, June 1991, pp.374-380.

[8] Pulliam, T. H., "Time Accuracy and the Use of Implicit Methods," AIAA Paper 93-3360-CP, July 1993.

[9] Obayashi, S. and Wada, Y., "Practical Formulation of a Positively Conservative Scheme," *AIAA Journal*, Vol. 32, 1994, pp. 1093-1095.

[10] Anderson, W. K., Thomas, J. L. and Van Leer, B., "A Comparison of Finite Volume Flux Vector Splittings for the Euler Equations," AIAA Paper 85-0122, Jan. 1985.

[11] Venkatakrishnan, V., "Preconditioned Conjugate Gradient Methods for the Compressive Navier-Stokes Equations," *AIAA Journal*, Vol. 29, No. 7, July 1991, pp.1092-1100.

[12] Venkatakrishnan, V., "On the Accuracy of Limiters and Convergence to Steady State Solutions," AIAA Paper 93-0880, Jan. 1993.

[13] Baldwin, B. S. and Lomax, H., "Thin-Layer Approximation and Algebraic Model for Separated Turbulent Flows," AIAA Paper 78-257, Jan. 1985.

[14] Pulliam, T. H., "Implicit Solution Methods in Computational Fluid Dynamics," *Applied Numerical Mathematics*, Vol. 2, 1986, pp. 441-474.

[15] Brant, A., "Multi-Level Adaptive Solutions to Boundary Value Problems," *Mathematics of Computation*, Vol. 31, No. 138, April 1977, pp.333-390.

[16] Case, J., Chilver, A. H. and Ross, C. T. F., *Strength of Materials & Structures with an Introduction to Finite Element Methods*, 3rd Edn., Edward Arnold, London, 1993.

[17] Nakamura, T., Iwamiya, T., Yoshida, M., Matsuo, Y., and Fukuda, M., "Simulation of the 3 Dimensional Cascade Flow with Numerical Wind Tunnel (NWT)," *Proceedings of the 1996 ACM/IEEE Supercomputing Conference* [CD-ROM], Inst. of Electrical and Electronics Engineers Computer Society, Washington, DC, 1996.